A. Montorfano, F. Piscaglia, A. Onorati
A Les Study on the Evolution of Turbulent Structures in Moving Engine Geometries by an Open-Source CFD Code
SAE TECHNICAL PAPER, Vol. 1, SAE Technical Paper 2014-01-1147, 2014, p. 1-15
doi:10.4271/2014-01-1147

2014-01-1147

A LES Study on the Evolution of Turbulent Structures in Moving Engine Geometries by an Open-Source CFD Code

A. Montorfano, F. Piscaglia, A. Onorati
Dipartimento di Energia, Politecnico di Milano, Italy

Abstract

The dynamics and evolution of turbulent structures inside an engine-like geometry are investigated by means of Large Eddy Simulation. A simplified configuration consisting of a flat-top cylinder head with a fixed, axis-centered valve and low-speed piston has been simulated by the finite volume CFD code OpenFOAM®; the standard version of the software has been extended to include the compressible WALE subgrid-scale model, models for the generation of synthetic turbulence, some improvements to the mesh motion strategy and algorithms for LES data post-processing. In order to study both the initial transient and the quasi-steady operating conditions, ten complete engine cycles have been simulated. Phase and spatial averages have been performed over cycles three to ten in order to extract first and second moment of velocity; these quantities have then been used to validate the numerical procedure by comparison against experimental data. Complex unsteady features of turbulent fields like laminar-to-turbulent transition and tumble vortexes evolution have been studied either by time-resolved analysis and Proper Orthogonal Decomposition (POD). In addition, the cycle-to-cycle variations of flow field due to turbulent unsteadiness has been investigated by statistical analysis. Despite the present study has been carried out on a simplified geometry, it shows that LES can be a reliable tool not only for predicting averaged quantities (mean velocity and Reynolds stresses), but also to reproduce the dynamic behavior of complex turbulent structures in IC engines.

Introduction

Among all physical phenomena that occur inside an engine cylinder, turbulence has certainly a direct impact on thermodynamic efficiency, brake power and emissions of the engine since its influence extends from volumetric efficiency to air/fuel mixing, combustion and heat transfer. Historically, turbulent flows have been simulated mainly by models based on Reynolds Averaging of Navier-Stokes equations (RANS), either in they original version or in the unsteady formulation (URANS) for slowly-varying flows [1]. In ICE simulation, URANS approaches have proved to provide very good predictions of phase-averaged flow fields: macroscopic features of charge motion – like swirl and tumble vortexes – can be estimated with a good accuracy [2]. On the other hand, most of the time-varying quantities characterizing in-cylinder flows cannot be resolved by a model based on implicit time- or ensemble-averaging methods like URANS: small-scale turbulence, cycle-to-cycle variability (CCV) and in-cycle evolution of three-dimensional structures (jets and vortexes) can be simulated only by a time-resolved (rather than time-averaged) approach like Large Eddy Simulation (LES) [3]. In the recent years, LES has been successfully applied to ICE simulation by several authors, including Haworth [4, 5], Thobois *et al.* [6, 7], Hasse *et al.* [8]; their work has shown that good predictions of mean and fluctuating velocity, together with estimation of turbulence-driven CCV, can be achieved by LES.

The aim of this paper is to further explore the potentiality of LES for ICE simulation. The computational tool used in this paper is the open-source CFD software OpenFOAM® [9], whose current standard version (2.2.x) has been extended by the authors to include the new features [10, 11, 12, 13, 14] used for the present work. In particular, modifications regarded the inclusion in the code of compressible WALE subgrid-scale model [15], some improvements to the mesh motion strategy, and suitable boundary and initial conditions for LES which includes turbulent structures (generated artificially at the boundary), with physically sound spatial and temporal correlations [16]. Finally, algorithms for data post-processing, such as for the calculation of Proper Orthogonal Decomposition (POD), have been developed. The implemented framework for LES has been included in LibICE, a C++ open-source library for ICE simulation developed at Politecnico di Milano.

The paper is organized as follows: first the simulated geometry will be presented together with the numerical setup, then a basic validation of the procedure by comparison against experimental data will be performed and the completeness of simulations will be assessed. Finally, a more thorough analysis of dynamic features is carried out and followed by a discussion upon the results.

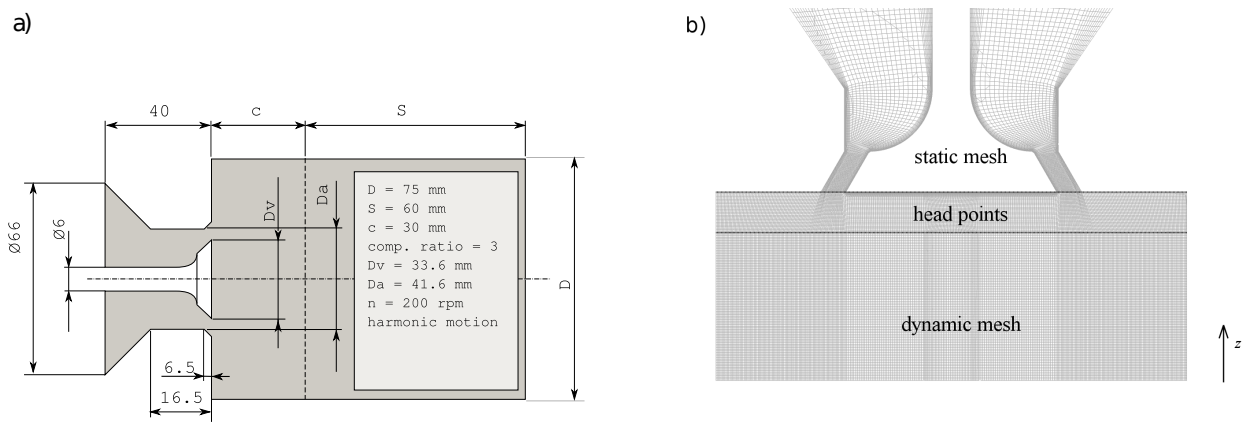

Figure 1: a) Geometry of the experimental apparatus used by Morse *et al.* [17]. The same configuration has been modeled for the present paper, with the addition of an upper plenum (not shown). b) Cut view of the Finite Volume grid used for the simulations. The whole mesh had about 4.8 million hexahedral elements, including the plenum (not shown).

Case setup

The axisymmetric piston-valve assembly introduced by Morse *et al.* [17] has been selected as a test-case for the present study. Specification of the geometry as well as a list of main functioning parameters are represented in Fig. 1. The piston has a bore diameter of 75 mm and stroke is 60 mm. Clearance height is 30 mm from cylinder head, thus geometric compression ratio is 3. The poppet valve is coaxial with respect to the piston axis and it remains at fixed height through the whole engine cycle. Piston motion is purely harmonic with a frequency of 200 rpm; as a consequence, the engine Reynolds number (considering air as a working fluid) is $\mathrm{Re} = \rho \overline{U}_p D/\mu = 2000$.

The geometry has been discretized with a pure structured hexahedral mesh, which is depicted in Fig. 1-b. The cylinder inlet section is connected to a plenum (not represented) whose volume is about 15 times the cylinder volume. The purpose of the plenum is to avoid reflections from the boundaries and thus improve the stability of the simulation. The total number of elements in the mesh is approximately 4.8 million, with a minimum cell thickness of about 0.02 mm in the valve seat.

Dynamic mesh handling has been based on a point motion strategy without topological changes. Mesh points have been divided into three sets according to the motion law they were subjected to (see Fig. 1-b). All points above the cylinder head are fixed since there are no moving boundaries there; as a consequence, they belong to the set named “static mesh” and their displacement velocity is zero everywhere. Similarly, points located below the cylinder head (“head points” in Fig. 1-b) were not moving to preserve the cell quality in a critical region like the interface between valve seat and cylinder. Finally, points belonging to the cylinder region (with the exception of the “head points” just mentioned) do move axially to account for the deforming geometry. In this work the cylinder axis was aligned to the z axis of the global reference frame (Fig. 1); the following relations are therefore written accordingly. Given $\boldsymbol{U}_p$ as the piston velocity ($\boldsymbol{U}_p(t) = S/2 \sin(\omega t)\boldsymbol{i}_c$; where S is the piston stroke and $\boldsymbol{i}_c$ the unit vector parallel to cylinder axis), the point velocity $\boldsymbol{u}_p$ is calculated as:

$$\boldsymbol{u}_p(\boldsymbol{x}_p) = \boldsymbol{U}_p \cdot \frac{z_{\mathrm{max}} - z_p}{z_{\mathrm{max}} - z_{\mathrm{piston}}} \tag{1}$$

where $\boldsymbol{x}_p = (x_p, y_p, z_p)$ is the point position, z_{max} is the z-coordinate of the farthest moving point from the cylinder and z_{piston} is the z-coordinate of the piston.

Subgrid-scale model

In this work, the WALE (Wall-Adapting Local Eddy-viscosity) model (first developed by Nicoud *et al.* [15]) has been implemented according to its compressible formulation [18]. The model is based on the eddy-viscosity assumption for compressible flows [19]:

$$\tau_{ij}^{sgs} = \mu_{sgs}\left(2\tilde{S}_{ij} - \frac{2}{3}\tilde{S}_{mm}\delta_{ij}\right) - \frac{2}{3}\bar{\rho}k^{sgs}\delta_{ij} \tag{2}$$

where τ_{ij} is the subgrid scale viscous stress tensor and $\tilde{S}_{ij}$ is the Favre-filtered strain rate tensor

$$\tilde{S}_{ij} = \frac{1}{2}\left(\frac{\partial \tilde{u}_i}{\partial x_j} + \frac{\partial \tilde{u}_j}{\partial x_i}\right) \tag{3}$$

The overbar denotes space filtered quantities, while the tilde denotes the Favre-filtered quantities. For most of the eddy-viscosity models, the eddy-viscosity can be written in the general formulation:

$$\mu_{sgs} = C_m^2 \, \bar{\rho} \, \bar{\Delta}^2 \, \widetilde{OP}(\boldsymbol{x}, t) \tag{4}$$

where C_m is the constant of the model, $\bar{\Delta}$ is the filter characteristic length scale (calculated as $\bar{\Delta} = V^{1/3}$, where V is the local cell volume) and $\widetilde{OP}$ is an operator of space and time, homogeneous to a frequency, defined from the resolved fields.

For the compressible case, the resulting formulation for the eddy viscosity is:

$$\begin{aligned}\mu_{sgs} &= \bar{\rho}\left(C_w\bar{\Delta}\right)^2 \frac{\widetilde{OP}_1}{\widetilde{OP}_2} \\ &= \bar{\rho}\left(C_w\bar{\Delta}\right)^2 \frac{\left(s_{ij}^d s_{ij}^d\right)^{\frac{3}{2}}}{\left(\tilde{S}_{ij}\tilde{S}_{ij}\right)^{5/2} + \left(s_{ij}^d s_{ij}^d\right)^{5/4}}\end{aligned} \tag{5}$$

where s_{ij}^d is the traceless symmetric part of the square of the velocity gradient tensor $\bar{g}_{ij} = \partial u_i / \partial x_j$:

$$s_{ij}^d = \frac{1}{2}\left(\tilde{g}_{ij}^2 + \tilde{g}_{ji}^2\right) - \frac{1}{3}\delta_{ij}\tilde{g}_{kk}^2 \tag{6}$$

In order to write the subgrid-scale viscous stress tensor, the relation between the turbulent viscosity μ_{sgs} (see Eq. 4) and the turbulent subgrid scale kinetic energy k^{sgs} must be considered:

$$\begin{aligned} k^{sgs} &= C_2 \bar{\Delta}^2 \, \tilde{S}_{mn}\tilde{S}_{mn} = C_2 \bar{\Delta}^2 \, \left(\frac{\mu_{sgs}}{\bar{\rho}\, C_m^2 \, \bar{\Delta}^2}\right)^2 \\ &= C_w' \, \left(\frac{\mu_{sgs}}{\bar{\rho}\, \bar{\Delta}}\right)^2 \end{aligned} \tag{7}$$

By the combination of Eq. (7) and Eq. (2) it follows:

$$\tau_{ij}^{sgs} = 2\mu_{sgs}\left(\tilde{S}_{ij} - \frac{1}{3}\tilde{S}_{mm}\delta_{ij}\right) - \frac{2}{3}\frac{C_w'}{\bar{\rho}}\left(\frac{\mu_{sgs}}{\bar{\Delta}}\right)^2 \delta_{ij} \tag{8}$$

As suggested in [18], C_w' has been set to 45.8. To make the stress realizable, its diagonal entries were forced to be nonpositive.

Among the favourable characteristics of the WALE model, that make it very suitable for engine flows, one has:

- invariance to any coordinate translation or rotation;
- ease of implementation on any kind of computational grid;
- it is function of both the strain and the rotation rates;
- it goes naturally to zero at the wall with y^3 behavior, so that neither damping function nor dynamic procedure are needed to reproduce the effect of the no-slip condition at the wall.

The WALE SGS model had be implemented by the authors of the present work in the OpenFOAM® technology; both the implementation and the suitability for engine-like cases have been assessed in previous works [12, 20].

Numerical setup

The compressible filtered Navier-Stokes equations have been solved using a Finite Volume (FV) solver based on the transient-SIMPLE algorithm [21]; this choice has been driven by the necessity of ensuring convergence of pressure-velocity coupling at each timestep without being limited by the Courant-Friedrichs-Lewis (CFL) criterion. Temporal integration has been performed with a fixed angular step equal to $\Delta\theta$ = 0.05°; as a consequence, the maximum Courant number ranged from 0.75 (near bottom- and top-dead-center) to $\approx$ 11 around $\theta = 90° + \mathrm{k}\,180°$, with $\mathrm{k} = [0; \mathrm{N_{cycles}}]$. A total number of 10 piston cycles have been simulated, even though only data from the last 8 cycles have been used for postprocessing. Time derivatives have been discretized using a second-order backward differencing scheme, while pure second-order differencing has been used on all space derivatives with the exception of the momentum advection ($\nabla\cdot(\rho\boldsymbol{UU})$). For this term, an interpolation scheme in which linear-upwind is blended with linear interpolation has been used with a blending factor of 75% linear [22], in order to achieve a very stable solution with an almost second-order accuracy. Boundary conditions at the walls were set as adiabatic. Wall functions were not applied at the solid walls: flow equations were solved up to $y^+ \to 0$, despite it was known that mesh resolution was not sufficient to solve the boundary layer. Synthetic-turbulence at the inlet boundary [13, 23] was generated for the flow entering into the domain, while a non-reflecting condition on pressure was applied for the outgoing flow.

Post-processing of results

Post-processing of results is an important part of every analysis based on LES. The large amount of data coming from the computation needs to be reduced to extract usable information. Usually, the first stage of data processing consists in the calculation of first and second statistical moments of velocity: in this case the reduction algorithm discards any dynamic information about the flow field. Averaging has been applied in this work to compare mean and RMS velocity profiles against experimental measurements, in order to validate the simulation procedure.

On the other hand, CCV is usually detected and measured on the basis of some quantities obtained by an integration over the volume, that are examined as they evolve through the different engine cycles. In this paper the chosen measure for CCV is the specific kinetic energy:

$$\langle \bar{E}(t) \rangle = \iiint \frac{1}{2}\widetilde{u}(\boldsymbol{x},t)\widetilde{u}(\boldsymbol{x},t)\mathrm{d}x\mathrm{d}y\mathrm{d}z \tag{9}$$

Finally, informations about the organized motions of the flow field and their energy content can be extracted by means of Proper Orthogonal Decomposition (POD). POD consists in decomposing a time-varying velocity field $\boldsymbol{u}(\boldsymbol{x},t)$ into M independent pairs $[a^{(k)}(t), \psi^{(k)}(\boldsymbol{x})]$, where $a^{(k)}(t)$ is a time-dependent coefficient expressing the energy content of the *k-th* mode, and $\psi^{(k)}(\boldsymbol{x})$ is the corresponding spatial basis function:

$$\boldsymbol{u}(\boldsymbol{x},t) = \sum_{k=1}^{M}\left[a^{(k)}(t)\psi^{(k)}(\boldsymbol{x})\right] \tag{10}$$

POD modes are usually extracted by the so-called "method of snapshots", that has been originally developed by Sirovich [24] to reduce the computational cost of formal methods [25]. Given a number of realizations M of a time-dependent vector field $\boldsymbol{u}(\boldsymbol{x},t)$, it is possible to define the inner product:

$$\left(\boldsymbol{u}^{(i)}, \boldsymbol{u}^{(j)}\right) = \sum_{n=1}^{N}\left[\sum_{d=1}^{D}\left[u_d^{(i)}(\boldsymbol{x}_n)u_d^{(j)}(\boldsymbol{x}_n)\right]\right] \tag{11}$$

Eq. (11) is used to build the matrix $\mathbf{C}$, where:

$$C_{ij} = \frac{\left(\boldsymbol{u}^{(i)}, \boldsymbol{u}^{(j)}\right)}{M} \tag{12}$$

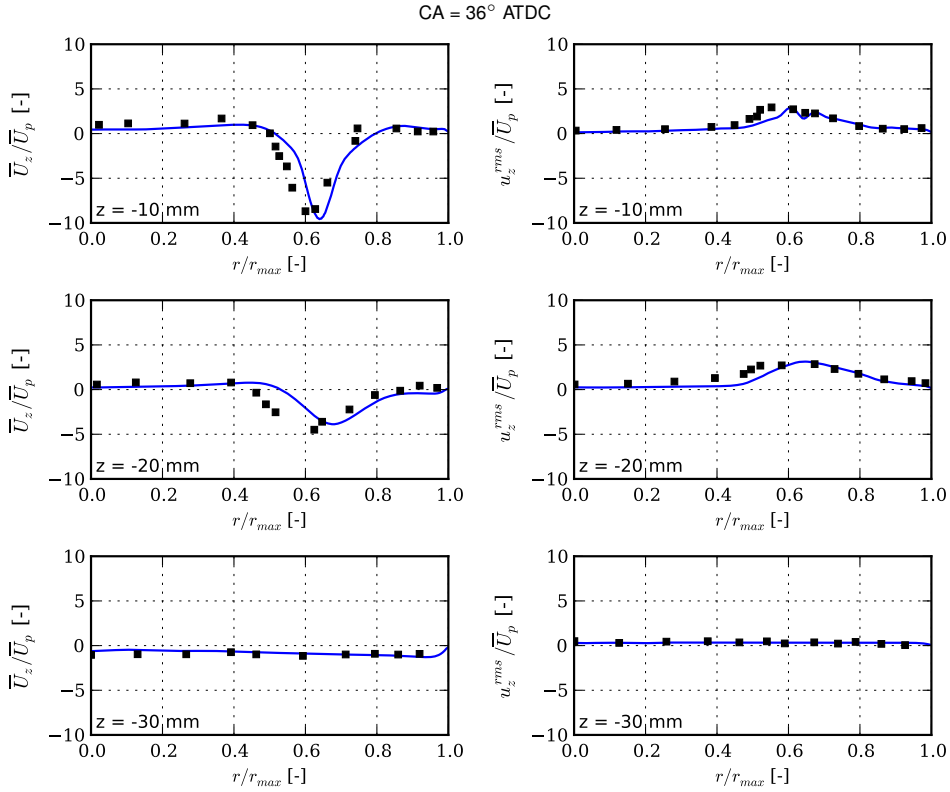

Figure 2: Profiles of mean axial velocity (left) and axial RMS fluctuations (right) for CA = 36° ATDC, at different distances from the cylinder head (conventionally $z = 0$). — simulations; ■ experiments.

for which the following eigenvalue problem is solved:

$$\mathbf{C}\,\boldsymbol{q}^{(k)} = \lambda^{(k)}\boldsymbol{q}^{(k)} \tag{13}$$

Finally, the POD modes are calculated as:

$$\psi_d^{(k)}(\boldsymbol{x}_n) = \sum_{m=1}^{M} q_m^{(k)} u_d^{(m)}(\boldsymbol{x}_n) \tag{14}$$

and the time-varying coefficients as:

$$a^{(k)}(t) = \left(\boldsymbol{u}^{(i)}, \psi^{(k)}\right) \tag{15}$$

with i as the temporal index.

Usually, eigenvalues and eigenvectors resulting from Eq. (13) are ordered by decreasing magnitude of the eigenvalues, so that the energy content of POD modes $[\psi^{(1)} \ldots \psi^{(M)}]$ will be in decreasing order as well.

Since a reciprocating engine is characterized by a periodic operation due to its varying geometry, it is generally not appropriate to consider the temporal index i as $\theta = i\,\Delta\theta$ (being $\Delta\theta$ the integration step). One solution is to calculate a "phase-dependent" POD: for each crank-angle position a different POD is calculated, where the number of snapshots is defined by the total number of simulated engine cycles. It is worth mentioning that an alternative method is available, namely the "phase-independent" POD, where linear transformations are applied to the FV grid and to the velocity field for each crank-angle; the total number of realizations equals the number of saved timesteps. The "phase independent" POD has been developed by Fogleman *et al.* [26] and applied to the same test case of this paper by Liu and Haworth [27]. However, in the present work, the former approach has been chosen because, in the authors' opinion, it allows for a better physical insight on the dynamics of turbulence inside an engine cylinder.

Basic solver validation

In this section, the solver and setup used to simulate the configuration of Fig. 1 will be evaluated in order to validate the whole LES procedure. First, a comparison between mean and RMS velocities obtained by LES and the experimental measurements by Morse *et al.* [17] will be presented. A similar comparison was done in the direct numerical simulations in [28]. Afterward, the completeness of the simulation will be estimated by quantitative parameters.

Average and RMS velocity

Comparisons between simulated and measured data have been performed for three different Crank-Angle (CA) positions, namely, 36, 90 and 144 CA degrees. Both ensemble averaging and space averaging have been applied to the results. As mentioned before, only the last eight cycles, out of a total of ten, have been considered for the post-processing. This choice was due to the need of excluding any non-repeatable phenomenon that might occur during the very first phases of the simulation, when the cylinder

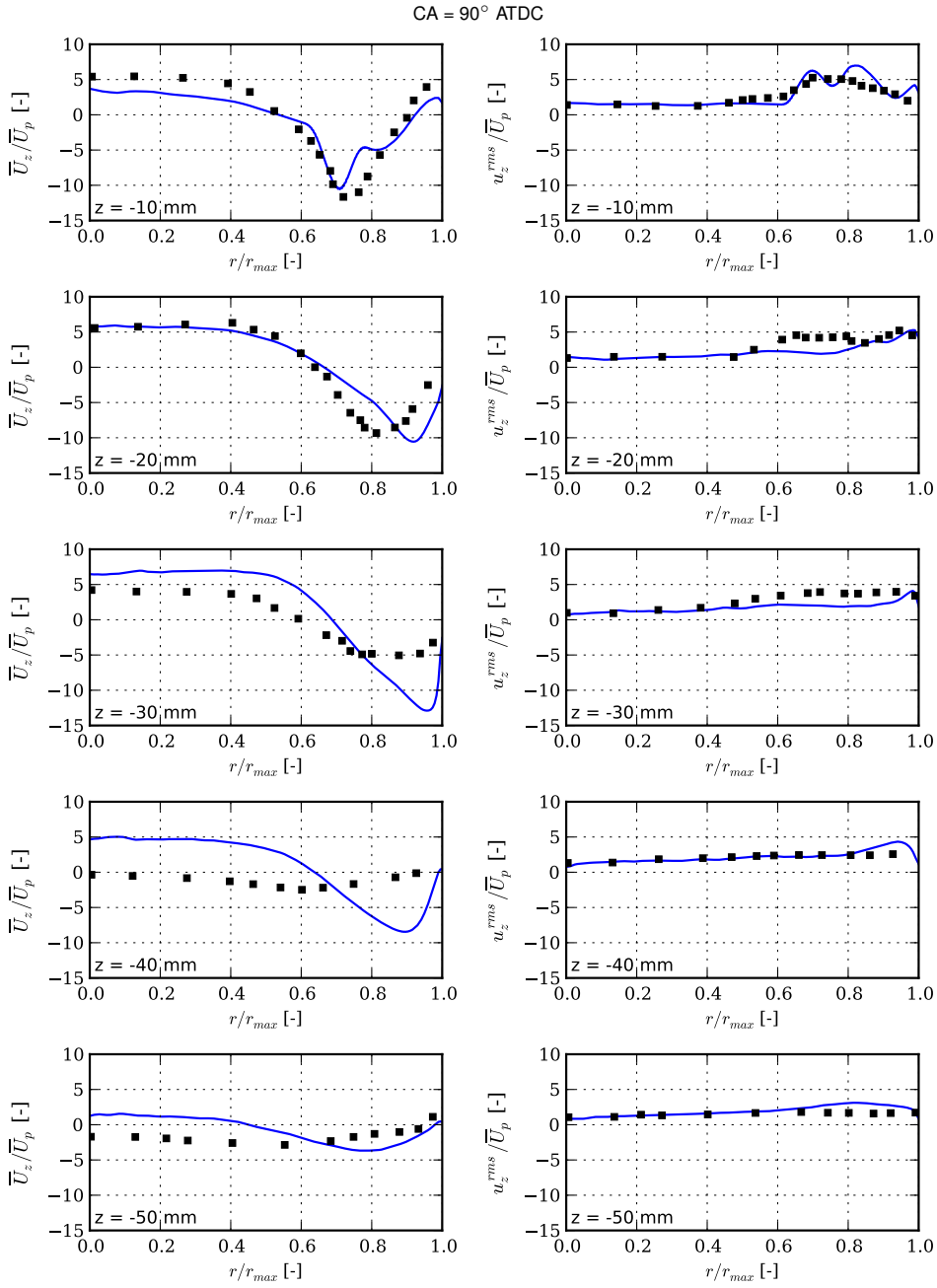

Figure 3: Profiles of mean axial velocity (left) and axial RMS fluctuations (right) for CA = 90° ATDC, at different distances from the cylinder head (conventionally $z = 0$). — simulations; ■ experiments.

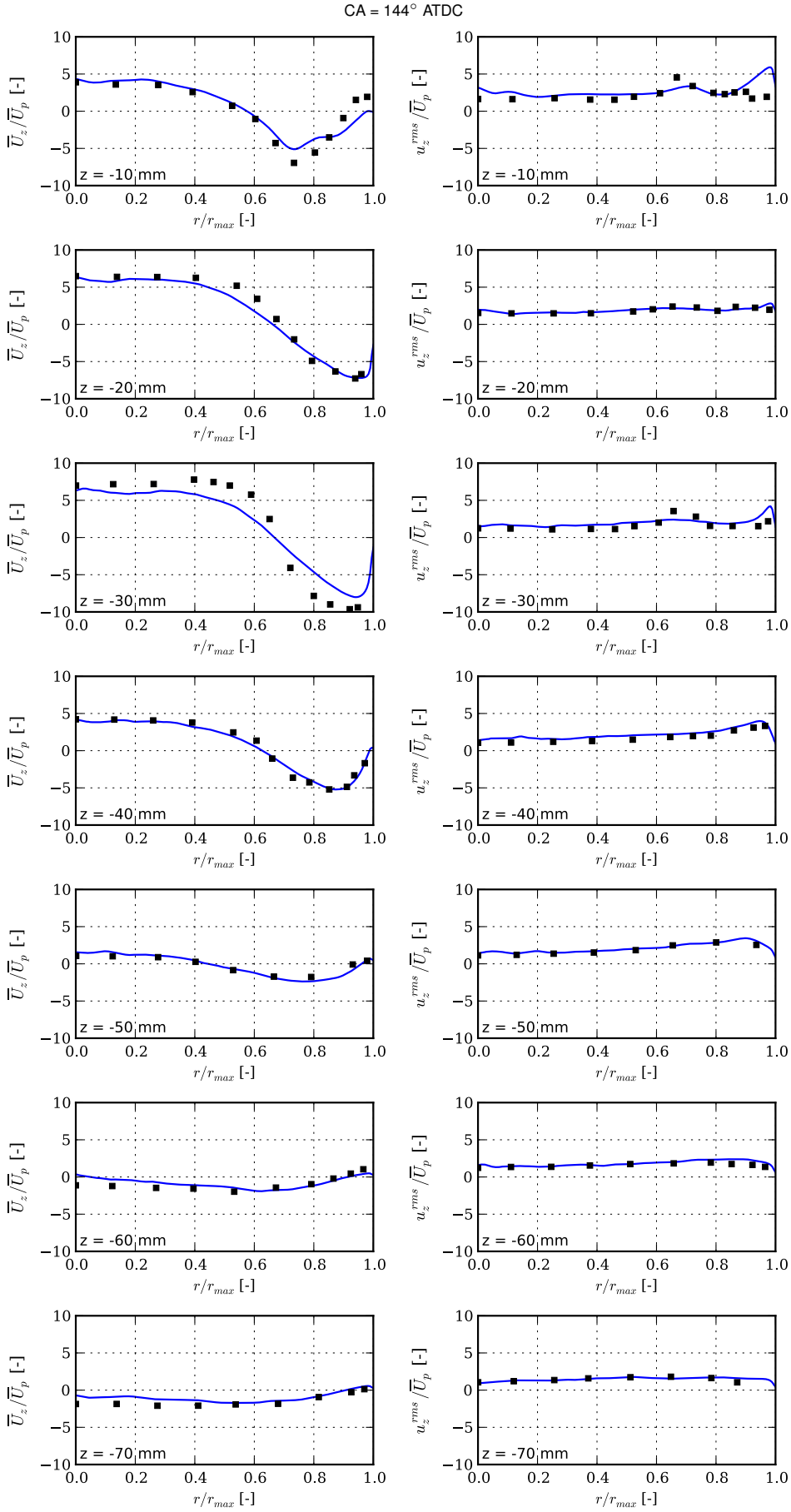

Figure 4: Profiles of mean axial velocity (left) and axial RMS fluctuations (right) for CA = 144° ATDC, at different distances from the cylinder head (conventionally $z = 0$). — simulations; ■ experiments.

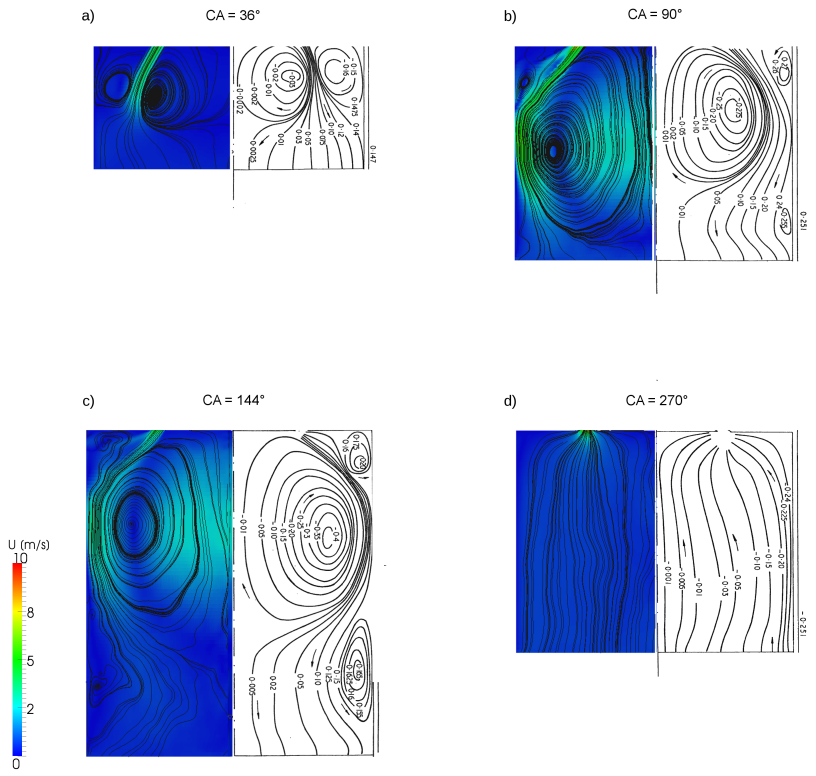

Figure 5: Comparison of simulated (left) and experimental (right) streamlines within the cylinder region at: a) CA = 36° ATDC; b) 90° ATDC; c) 144° ATDC; d) 270° ATDC.

conditions are very different with respect to the other cycles. Space averaging has been computed along the circumferential direction, in order to reduce the total number of engine cycles to be simulated. Data have been sampled with an angular step of 5°. Linear interpolation has been used to approximate the fields in between cell centers. Both ensemble averaged velocity ($\bar{U}$) and RMS fluctuations (u_z^{rms}) have been extracted from the circumferential-averaged planes and compared with experimental measurements. Profiles have been plotted along the cylinder radius at increasing distance (with a step $\Delta z = 10$ mm) from the cylinder head. Only the axial component of the velocity has been considered, since no reference data are available for the other two. In Fig. 2 velocity profiles for CA = 36° are represented. The match between simulation and experiments is very good on all sampling positions. The amplitude of local minima at z = -10 mm and z = -20 mm is correctly estimated, even though the position is slightly shifted towards the liner wall. The same considerations can be done for the local maxima of u_z^{rms}. At z = -30 mm velocities are very low, because the measurement location is very close to the piston. Comparison of averaged velocities at CA = 90° are represented in Fig. 3. The match between computed and measured values at z = -10 mm and z = -20 mm looks satisfying, the experimental profile is caught fairly well; the same observations made for the previous case apply to this crank angle position as well. However, differences between simulated and measured velocities increase as the sampling plane location is moved far from the cylinder head, even though the qualitative trend is generally preserved. On the other hand, RMS axial fluctuations are well predicted on all five sampling planes, both qualitatively and in absolute values. Predictions of velocity field for CA = 144° (Fig. 4) show a very good agreement with experimental data. Profiles of mean axial velocities are matched almost perfectly in all positions. Slight differences can be seen for RMS fluctuations near the cylinder walls; however, it is difficult to estimate the importance of such deviations since little information about the confidence interval of experimental data is available [17].
In Fig. 5 the streamlines stemming from simulation results (on the left) are combined with those obtained from experimental data by Morse et al. [17] (on the right). The purpose of this series of images is to provide a qualitative overview of the mean velocity field inside the cylinder. A comparison between simulations and experiments can be however done, bearing in mind that the simulated streamlines have been traced for different values of the stream-function with respect to experimental ones. At CA = 36° the match is very good both in terms of shapes and sizes of the recirculation regions, while at CA = 90° (Fig. 5-b) there is a mismatch in the size of the large recirculation vortex adjacent to the cylinder axis. A mismatch has been observed also in the two-dimensional plots already shown in Fig. 3; as it will be shown in the next paragraph, a possible explanation may be found in the mesh resolution that was used at CA = 90°, which is not sufficient to capture the main vortex structures influencing the flow field. However, at the same crank angle, similar discrepancies have been observed also in other au-

thors' works [5, 28]. At CA = 144° (Fig. 5-c) almost all flow features are caught, with some exception in the description of the corner vortex between the liner and the cylinder head; this structure is only hinted in the simulations and it cannot clearly be seen in the experiments. Finally, the streamlines plot at CA = 270° (represented in Fig. 5-d) does show only a uniform velocity field with parallel streamlines, due to the upward stroke of the piston.

Completeness estimate

A common issue with LES is to determine the maximum allowable cell size to resolve at least the 80% of total kinetic energy [1]. If the complete energy spectrum is not known from detailed experiments and/or DNS data, the completeness of the simulation has to be estimated in some way. In this work the Length Scale Resolution parameter (LSR) [29] has been adopted as an estimator of the mesh resolution. LSR is defined as:

$$\text{LSR} = \frac{\bar{\Delta}}{\ell_{DI}} \tag{16}$$

where ℓ_{DI} is the lower limit of the inertial sub-range, which is usually estimated as [1]:

$$\ell_{di} \simeq 60\,\eta \tag{17}$$

where η is the Kolmogorov scale. The LSR parameter is proportional to the ratio between the actual resolved energy level and the corresponding lower limit of the inertial sub-range: where the LSR value is equal to 1 all the turbulent scales up to the dissipation range are resolved. By the LSR definition, the evaluation of the actual resolved energy level is directly linked to the local filter size. It helps to clearly correlate the adopted mesh size to the local energy resolution all over the computational domain. In [12, 30], a LSR value between three and five is given as the upper limit to guarantee a reasonable LES resolution at an affordable computational cost.

The common use of a completeness estimator is to detect the mesh regions that need a local refinement. However, when the mesh is dynamically changing, it is important also to monitor the cell sizes during the whole simulation. In fact, it is possible that for some crank angles (most likely near bottom dead center), the LES filter width is too coarse to correctly resolve the turbulent scales. Contour plots of LSR for the first processed cycle are represented in Figs. 6. From the pictures it clearly appears that LSR is almost everywhere lower than the threshold value of 5. LSR is higher than 5 only at CA = 90°, in the shear layer between the annular jet and the in-cylinder region and on the liner walls where the jets impacts.

This helps to justify the discrepancy that has been noticed in Fig. 3 and Fig. 5 between the predictions and the experiments for this piston position; however, a maximum value of LSR of about 7 is not high enough to pose concerns about the quality of the overall simulation; the analysis of completeness shows that mesh resolution might be increased in the upper part of the cylinder, but it is fine enough to resolve up to the limit of the inertial subrange. As evidenced also in [12], the LSR parameter is very helpful when used

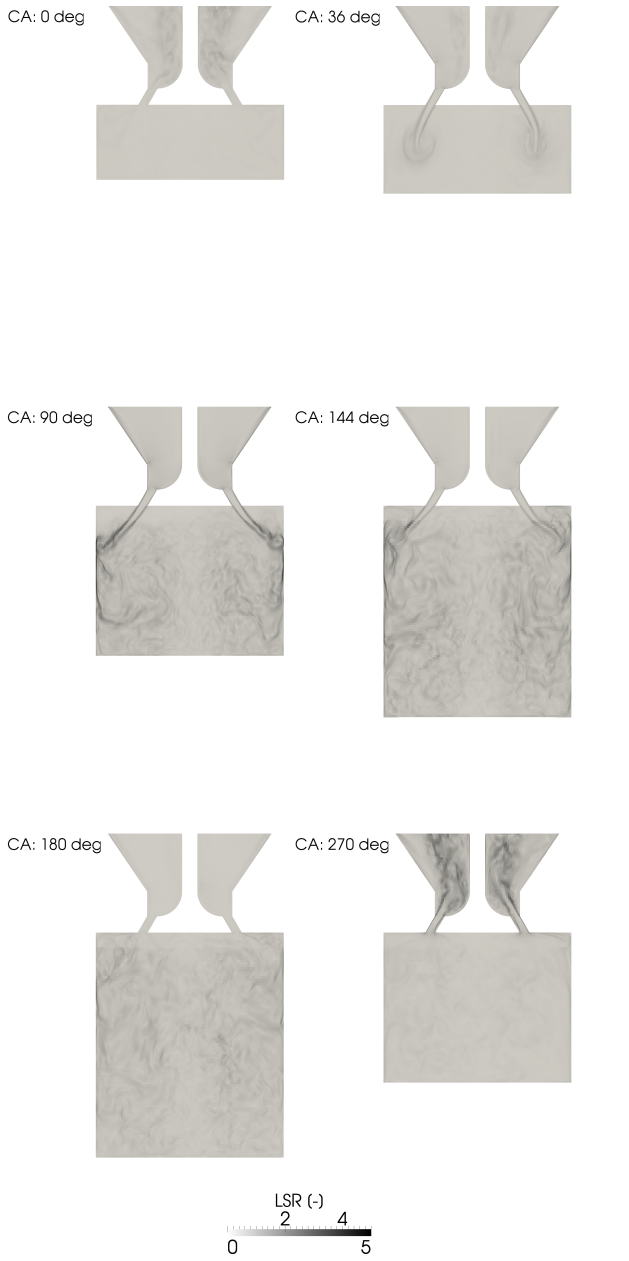

Figure 6: Contour plots of the LSR parameter on an axial plane. a) 0° (TDC); b) 36° ATDC; c) 90° ATDC; d) 144° ATDC; e) 180° ATDC; f) 270° ATDC. LSR looks higher than 5 only at CA = 90°, in the shear layer between the annular jet and the in-cylinder region and on the liner walls where the jets impacts.

to compare similar grids having different refinement levels; this is a consequence of the fact that in similar grids the filters are related to similar characteristic lengths and are therefore comparable. Conversely, when different grids are compared (structured with unstructured, unstructured with hybrid, different unstructured), LSR represents only a qualitative parameter, to distinguish between mesh zones that are refined enough and zones whose resolution is not sufficient to describe the main turbulent structures characterizing the physics to study.

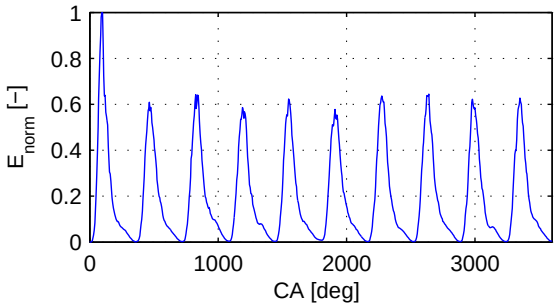

Figure 7: Volume integral of resolved kinetic energy $\langle \bar{E}(\theta) \rangle$ versus global crank-angle.

Further results and discussion

Cycle-to-Cycle Variability

The most promising aspect of LES is the capability of predicting unsteady flow phenomena, rather than average quantities like those used for validation. In Fig. 7, the normalized value of the integrated kinetic energy E, as defined in Eq. (9), is plotted against global crank angle for the cylinder region. The quasi-periodic trend is clearly recognizable; cycle-to-cycle variation is present, and it is especially apparent at the local maxima, when $\theta \approx 120^\circ + k\,360^\circ$. In particular, the difference in absolute value between the highest peak (which belongs to cycle n. 7) and the lowest one (cycle number 5) amounts to nearly 12%.

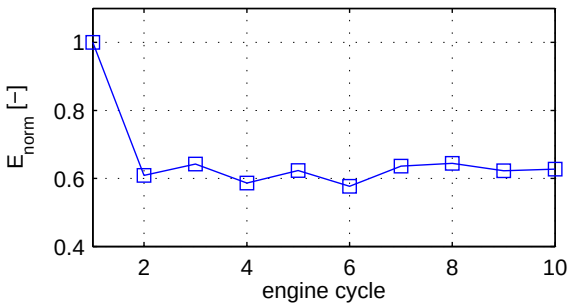

Figure 8: Maximum per-cycle value of $\langle \bar{E}(\theta) \rangle$

On the other hand, it does not seem to exist any monotone trend regarding the peak values of kinetic energy, see Fig. 8. With the exception of the first cycle, which has the highest absolute value, all other data points lie around the average value of E $\approx$ 0.675. However, Fig. 8 suggests also that some sort of cycle-to-cycle periodic phenomena might be present. In effect, starting from number 2, each cycle with an high value of peak kinetic energy is followed by a cycle with a low-value of it, and vice-versa.

In Fig. 9 the value of kinetic energy vs. crank angle is represented for each simulated cycle. Apart from cycle 1, the other curves are, more or less, overlapping. The largest CCV variation is seen to be around θ = 120°, in correspondence to the maximum values of E. A quantitative measure for that is given by the normalized standard deviation of the energy, Fig. 10. CCV is seen to be high during the in-

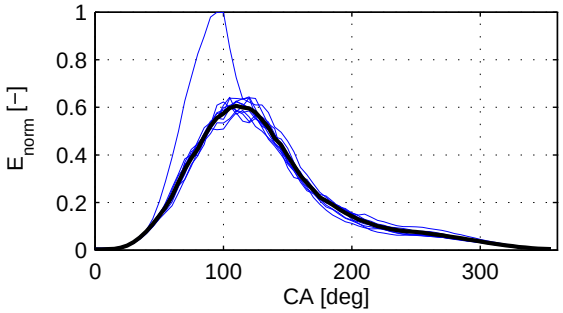

Figure 9: Cycle-to-Cycle Variability of $\langle \bar{E}(\theta) \rangle$ versus engine crank angle. — simulations; — average over eight engine cycles (3 to 10).

take stroke, with the peax value around 120° as already mentioned, but also with a small *plateau* in proximity of the bottom dead center. As expected, CCV is instead very low near the Top Dead Center, where turbulence level is at its minimum too.

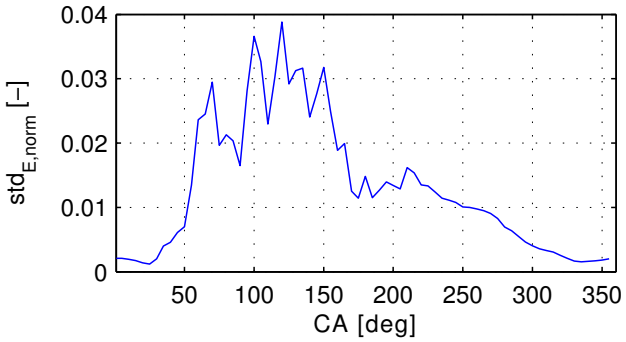

Figure 10: Variance of $\langle \bar{E}(\theta) \rangle$ calculated over eight engine cycles (3 to 10).

In order to gain a more detailed insight on the possible causes of CCV, the instantaneous vorticity field has been calculated at selected crank positions and contours of the absolute value of vorticity $|\boldsymbol{\omega}|$ have been plotted on vertical planes passing through the cylinder axis. In Fig. 11 the vorticity field at TDC is represented; as it might be expected, there are little or no organized structures at all, since they have been pushed into the upper plenum by the compression stroke. When the intake stroke begins, at CA = 36°, the annular jet coming from the valve enters into the cylinder (Fig. 12); a shear layer forms between the jet and the (relatively) undisturbed region that surrounds it, until the jet breaks up, at about mid-way between the cylinder head and

the piston. Some degree of CCV can be seen already at this stage, in particular looking at the shear vortexes at the end of the annular jet. In even cycles (cycles 4, 6, 8, 10) the diameter of the vortex is slightly larger with respect to odd cycles(cycles 5, 7, 9). At CA = 90°, vortical structures are fully developed and CCV is more clearly visible, especially in cycles from five to ten, see Fig. 13. Furthermore, there is a clear alternating pattern between odd and even cycles, that follows the trend already seen for CA = 36°. In fact, odd cycles have a vorticity field that is shifted towards the piston face, with a relatively calm region in the upper half of

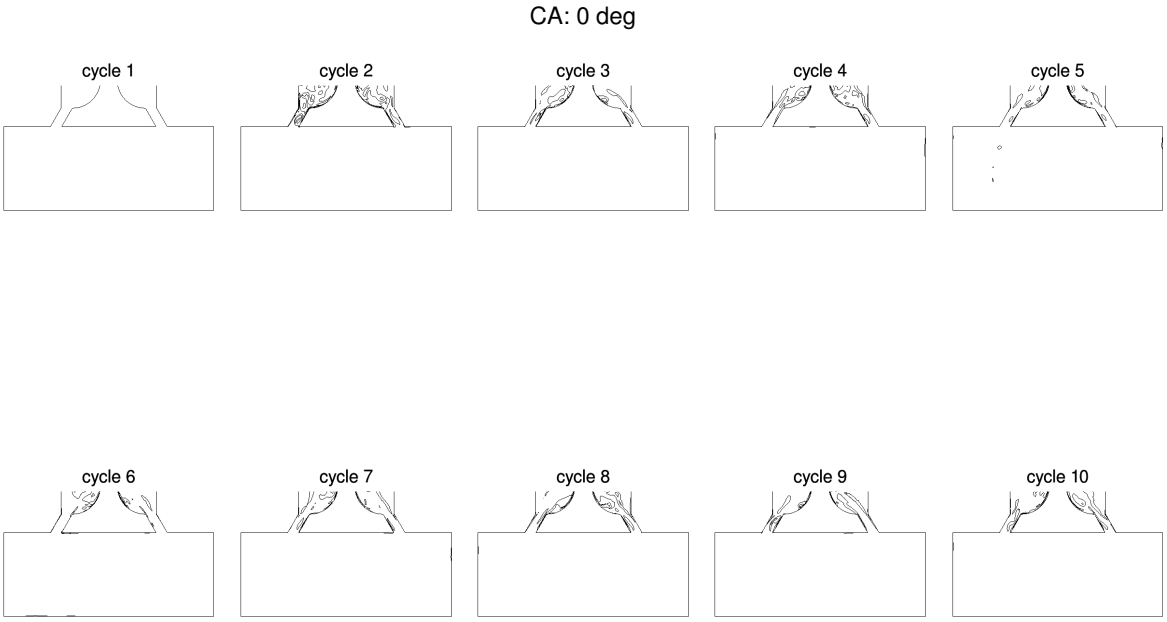

Figure 11: Vorticity contours at Top Dead Center for all simulated cycles

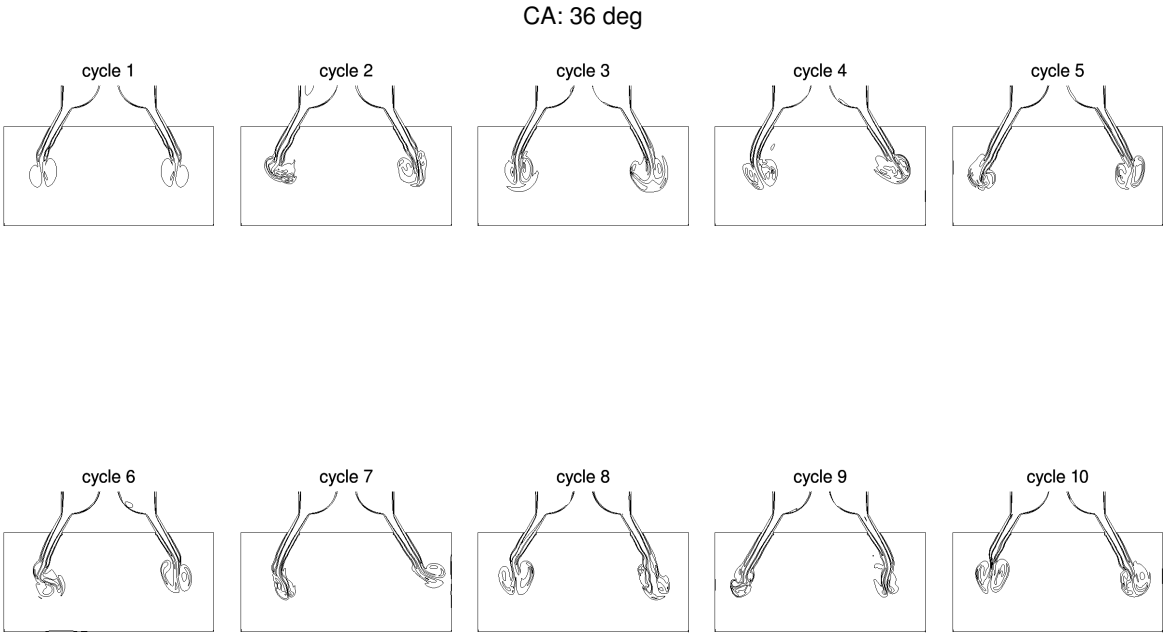

Figure 12: Vorticity contours at CA = 36° ATDC for all simulated cycles

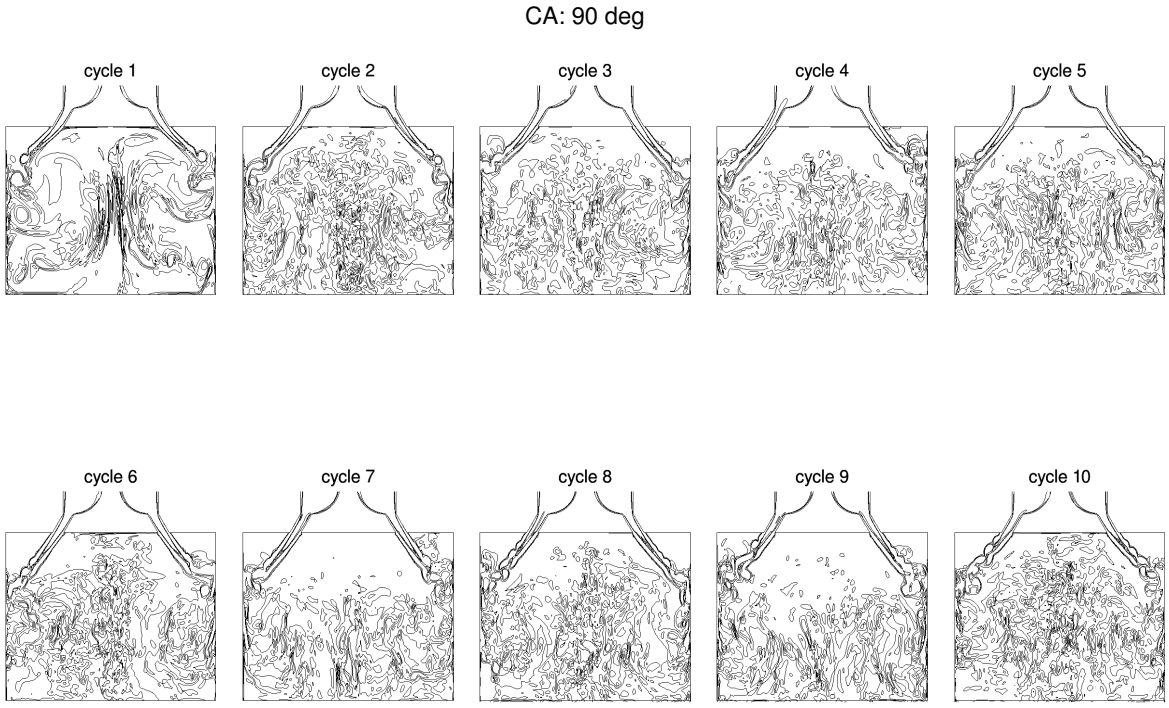

Figure 13: Vorticity contours at CA = 90° ATDC for all simulated cycles

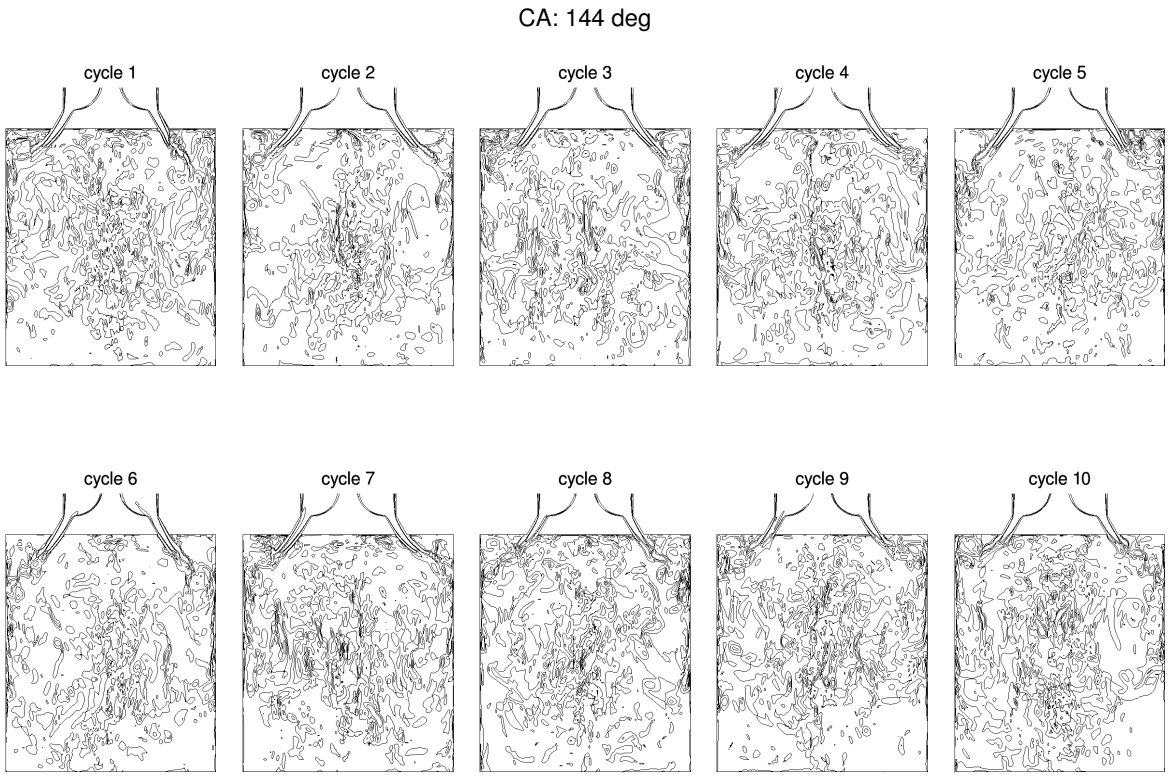

Figure 14: Vorticity contours at CA = 144° ATDC for all simulated cycles

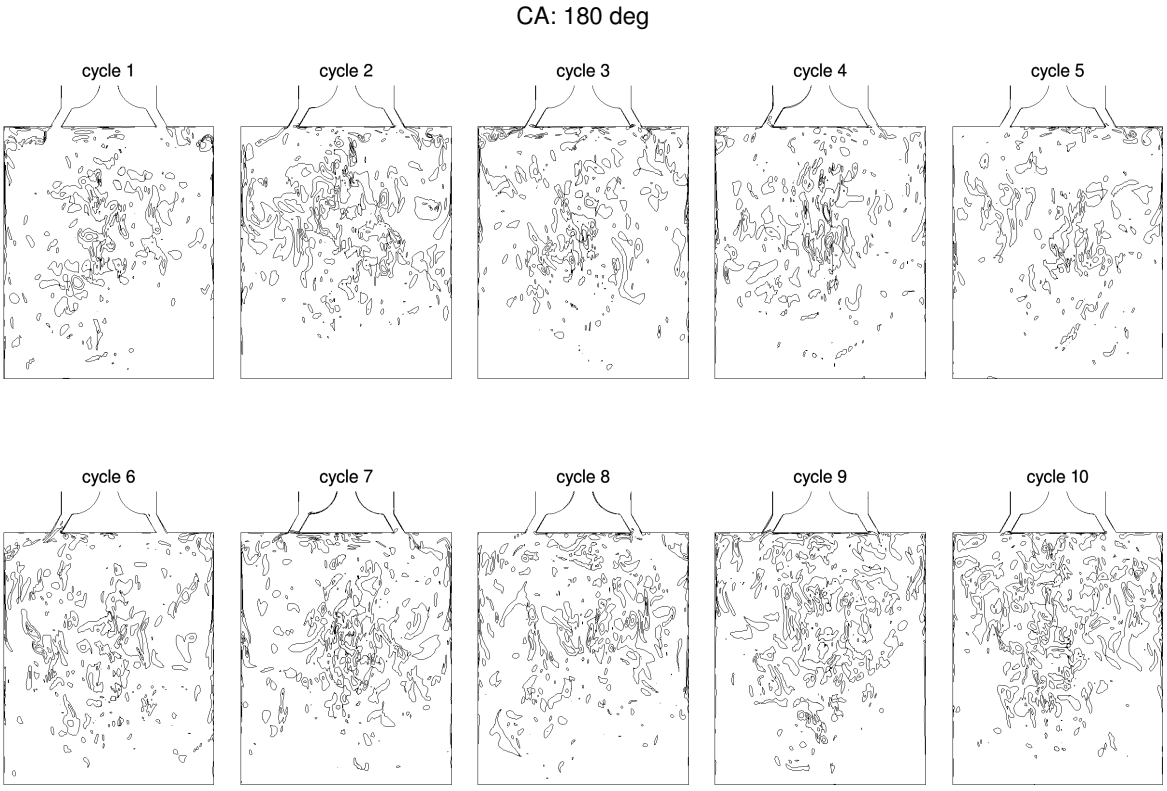

Figure 15: Vorticity contours at Bottom Dead Center for all simulated cycles

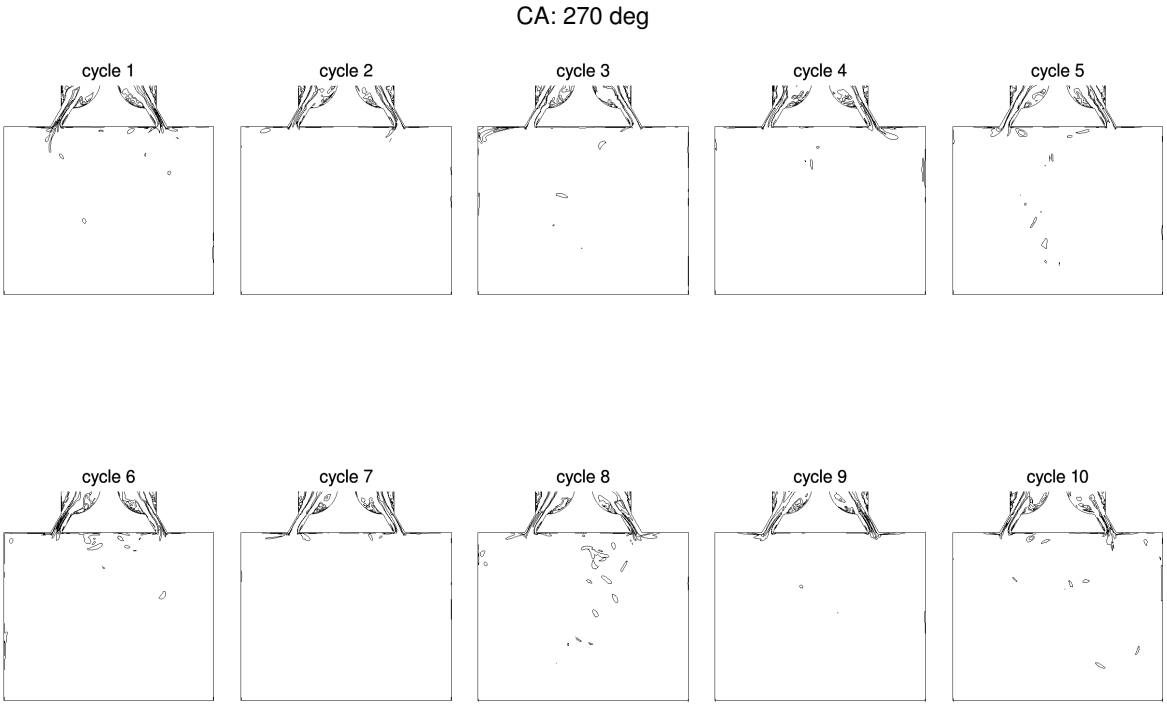

Figure 16: Vorticity contours at CA = 270° ATDC for all simulated cycles

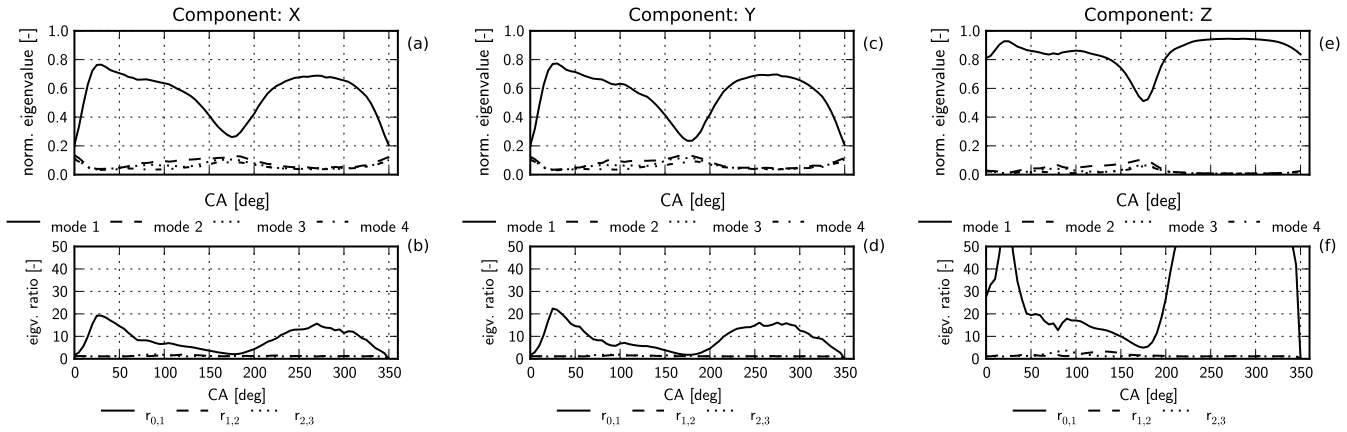

Figure 17: (a), (c), (e) Eigenvalues of POD modes versus crank angle for velocity component u_x, u_y and u_z. (b), (d), (f) Ratios between eigenvalues for velocity component u_x, u_y, u_z.

the cylinder. On the other hand, even cycles have a more uniform vorticity distribution, that extends nearly up to the valve. In addition, the shear layer instability in the jet coming from the valve section is clearly visible in these plots, especially for even cycles (six, eight and ten); in odd cycles ths instability is less evident and the jet breaks up with little or no sign of it. At CA = 144° (Fig. 14) the organized charge motion begin to dissipate since the fluid is not accelerated any more. As shown before, CCV is at its maximum around this crank angle position. The qualitative distribution of $|\boldsymbol{\omega}|$ is seen to change significantly among different snapshots on Fig. 14: however, there is no recognizable pattern as in the previous case. At BDC (Fig. 15) residual vorticity resides mainly near the cylinder axis but the motion is highly unorganized. After BDC the air is expelled from the cylinder into the plenum, so there are no visible vortical structures and streamlines are almost parallel to cylinder axis. This can be inferred also by Fig. 16 which depicts vorticity contour plots at CA = 270°.

POD analysis

To conclude the investigation of LES results, a phase-dependent POD analysis has been carried out. With the snapshots method, the number of extracted modes equals the number of saved timesteps; for a phase-dependend POD this is, in turn, the number of simulated engine cycles. By convention, modes are sorted in decreasing order of energy content, i.e., decreasing eigenvalue. Phase-dependent POD has been calculated on the whole domain, thus including the plenum. This must be taken into account when the results will be analyzed.

For the purposes of this section, only the first four modes are presented, out of a total of ten. In Figs. 17-a, 17-c and 17-e, each mode eigenvalues are represented for each velocity component, i.e. U_x, U_y, and U_z, respectively. In Figs. 17-b, 17-d and 17-f, the ratio $r_{i,i+1} = a_i/a_{i+1}$ between consecutive eigenvalues is displayed as well. This parameter can be regarded as an indicator of the level of organization of the flow: when $r_{i,i+1}$ is high, most kinetic energy is contained in first modes, whereas the remaining modes are less energetic. On the contrary, when $r_{i,i+1} \approx 1$ the energy is evenly distributed between modes.

The trend of the curves of mode 1 in Figs. 17-a, 17-c, 17-e reflects the variations of piston velocity. In fact, the curves have absolute minima at dead centers and local maxima around the middle of either the expansion and the compression stroke. Not surprisingly, due to the axisymmetric geometry, graphs concerning u_x and u_y (respectively Figs. 17-a and 17-c) are almost identical, whereas the curve related to u_z (Fig. 17-e) is shifted upwards, since the predominant direction of the flow is aligned with the z- axis, especially in the plenum region. In all graphs, the ratio $r_{1,2}$ between the first and the second eigenvalue is always significant, ranging from a minimum value of 2 (e.g. at dead centers for x-component) to a maximum of over 100 (e.g. at CA $\approx$ 270° for the z- component). On the contrary, the ratio between eigenvalues of greater order is much lower, being always comprised between 1 and 2. The first four modes extracted for piston at TDC are represented in Fig. 18-a. The unorganized character of the flow can be easily seen, since no large-scale structures can be detected. This situation is reflected by the low values of $r_{1,2}$ in Figs. 17-b and 17-d. However, since the flow has been pushed into the plenum, originating a strong upward jet, the value of $r_{1,2}$ related to u_z remains high. As the piston accelerates, and a jet is formed under the valve, the level of organization increases, especially with respect to u_x and u_y. At CA = 90° the eigenvalue ratios are higher, not only between the first two modes, but also among successive ones. In contour plots of Fig. 18-b the flow structures can be clearly recognized. Mode 1 has a strong resemblance to mean flow field (compare with average streamlines, Fig. 5), while higher modes 2 and 3 show smaller and smaller structures, that strongly remind the turbulence cascade from large to small eddies. At CA = 144°, that corresponds to the maximum degree of CCV, the first POD mode is still quite energetic, and its contour plot (Fig. 18-d) still has a strong affinity with the mean velocity field. However, the second mode has a smaller eddy length scale, with most part of energy concentrated in the jet shear layer. In mode 3 some vortical structures can be recognized, that were not in contours of mode 2. Both the main recirculation region and the ring vortex under the cylinder head can easily be detected. Finally, during the compression stroke, most turbulent features have been advected into the plenum

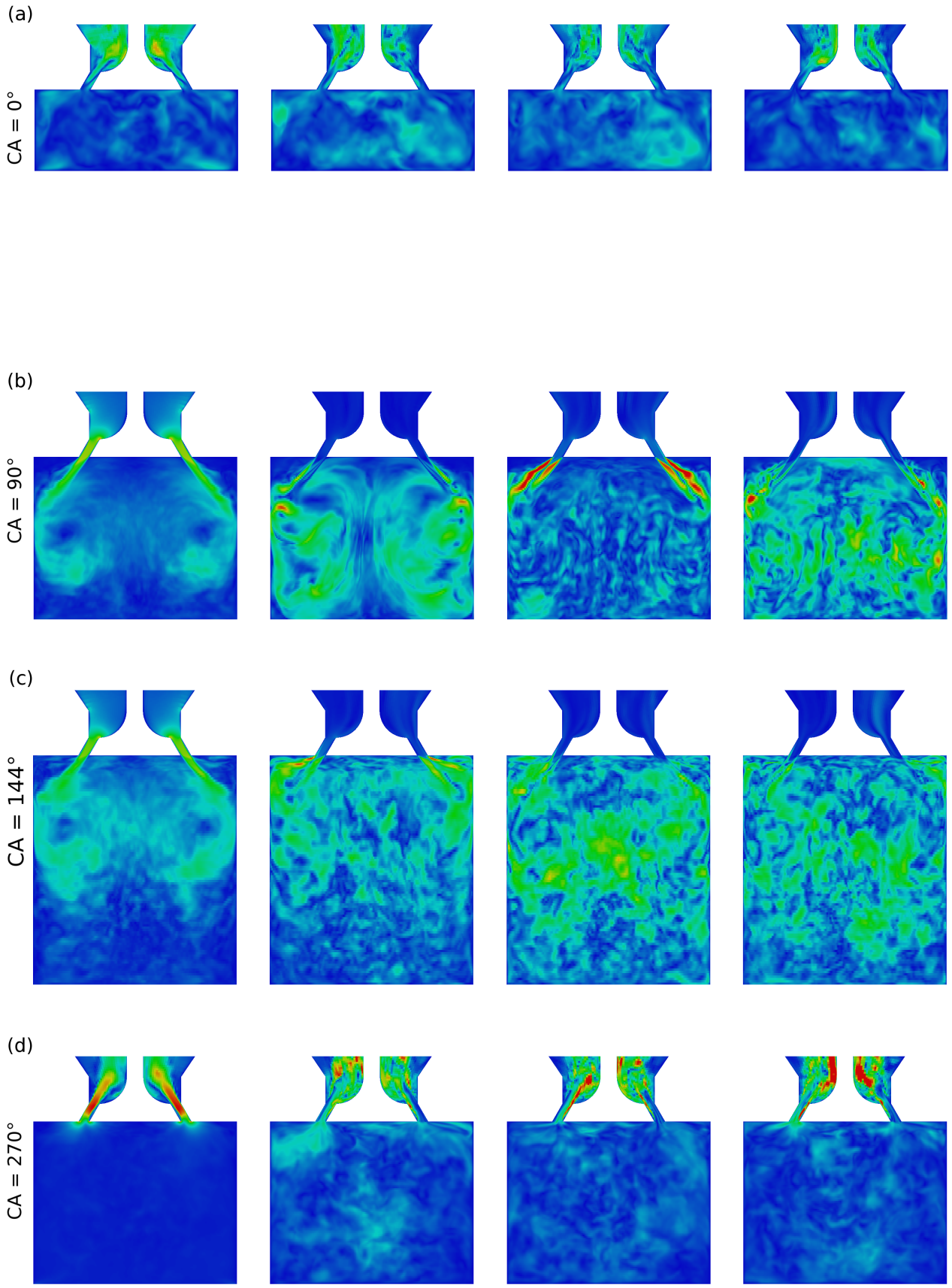

Figure 18: Magnitude of first four POD modes for varying crank-angles.

or dissipated by the upward motion of the piston. Thus, as one might expect, the contour plots of velocity modes do represent only small scales which almost have the same level of energy.

Conclusions

The purpose of this work was to validate and assess the capability of LES for predicting the turbulent behaviour of a compressible flow field within a deforming geometry. A simple engine-like geometry composed by a cylinder and an axisymmetric, fixed valve has been modeled and simulated by the CFD code OpenFOAM®-2.2.x. Extensions to the official version of the software regarded mainly the development of models for Large Eddy Simulation and of post processing tools, such as for phase and space averaging of fields and for the computation of phase-dependent POD.
The procedure presented proved to be accurate both in the prediction of average quantities and turbulence dynamics, while the LSR parameter proved to be reliable to identify if the grid resolution was sufficient to resolve the main turbulent scales of the engine. In particular, the analysis based on LSR allowed to justify the discrepancy between the predictions and the experiments found at 90° CA degrees in the shear layer, between the annular jet and the in-cylinder region and on the liner walls where the jets impacts. Cycle-to-Cycle Variability has been detected and the shear layer instability in the jet coming from the valve section, especially occurring at even cycles, has been shown. Finally, the POD analysis allowed for separating the energetic scales of unsteady motion, simplifying the study of turbulence evolution. The resulting level of detail of the proposed approach allows for a better insight on the unsteady phenomena occurring inside the cylinder, thus opening the way to a deeper understanding of physical bases of CCV.

Acknowledgments

The authors would like to acknowlege M. Schmitt and Dr. C. E. Frouzakis (Aerothermochemistry and Combustion Systems Laboratory, Swiss Federal Institute of Technology Zurich, Switzerland) and Prof. A. G. Tomboulides (University of Western Macedonia, Greece) for helpful discussions and for making available a draft of their manuscript [28].

References

[1] S. Pope, *Turbulent flows*. Cambridge University Press, 2000.

[2] A. Amsden, P. O'Rourke, and T. Butler, *KIVA-II: A Computer Program for Chemically Reactive Flows with Sprays*. LA 11560-MS, Los Alamos National Laboratory, 1989.

[3] P. Sagaut, *Large eddy simulation for incompressible flows: an introduction*. Scientific computation, Springer-Verlag, 2006.

[4] D. C. Haworth and K. Jansen, "Large-eddy simulation on unstructured deforming meshes: towards reciprocating IC engines," *Computers & Fluids*, vol. 29, pp. 493–524, 2000.

[5] K. Liu and D. C. Haworth, "Large-eddy simulation for an axisymmetric piston-cylinder assembly with and without swirl," *Flow, Turbulence and Combustion*, vol. 85, pp. 297–307, 2010.

[6] L. Thobois, G. Rymer, T. Soulères, and T. Poinsot, "Large-eddy simulation in IC engine geometries." Sae Paper n. 2004-01-1854, SAE world Congress & exhibition, 2004.

[7] L. Thobois, G. Rymer, T. Soulères, T. Poinsot, and V. den Heuvel B., "Large-eddy simulation for the prediction of aerodynamics in ic engines," in *Int. J. Vehicle Design "New strategies in Automotive Diesel Engines for Meeting Upcoming Pollutant Emission Restrictions"*, 2005.

[8] C. Hasse, V. Sohm, and B. Durst, "Numerical investigation of cyclic variations in gasoline engines using a hybrid URANS/LES modeling approach," *Computers & Fluids*, vol. 39, pp. 25–48, January 2010.

[9] The OpenFOAM Foundation, "`www.openfoam.org`."

[10] F. Piscaglia, A. Montorfano, and A. Onorati, "Development of a non-reflecting boundary condition for multidimensional nonlinear duct acoustic computation," *Journal of Sound and Vibration*, vol. 332, no. 4, pp. 922–935, 2013.

[11] F. Piscaglia, A. Montorfano, and A. Onorati, "Improving the simulation of the acoustic performance of complex silencers for ICE by a Multi-Dimensional non-linear approach," *SAE Int. J. Engines*, vol. 2, no. 5, pp. 633–648, 2012. doi:10.4271/2012-01-0828.

[12] F. Piscaglia, A. Montorfano, A. Onorati, and F. Brusiani, "Boundary conditions and subgrid scale models for LES simulation of IC engines." Accepted for publication on Oil & Gas Science and Technology – Revue d'IFP Energies nouvelles, 2013.

[13] F. Piscaglia, A. Montorfano, and A. Onorati, "Towards the LES simulation of IC Engines with parallel topologically changing meshes," *SAE Int. J. Engines*, vol. 6, no. 2, pp. 926–940, 2013.

[14] F. Piscaglia, A. Montorfano, and A. Onorati, "Development of fully-automatic parallel algorithms for mesh handling in the openfoam-2.2.x technology," *SAE Technical Paper 2013-24-0027*, 2013.

[15] F. Nicoud and F. Ducros, "Subgrid-scale stress modelling based on the square of the velocity gradient tensor," *Flow, Turbulence and Combustion*, vol. 62, pp. 183–200, 1999.

[16] A. Montorfano, F. Piscaglia, and G. Ferrari, "Inlet boundary conditions for incompressible les: A comparative study," *Mathematical and Computer Modelling*, 2011. doi:10.1016/j.mcm.2011.10.077.

[17] A. P. Morse, J. H. Whitelaw, and M. Yanneskis, "Turbulent flow measurements by laser-doppler anemometry in motored piston-cylinder assemblies.," *Journal of Fluids Engineering*, vol. 101, pp. 208–216, 1979.

[18] C. Wollblad, L. Davidson, and L.-E. Eriksson, "Large eddy simulation of transonic flow with shock wave/turbulent boundary layer interaction," *AIAA Journal*, vol. 44, pp. 2340–2353, 2006.

[19] E. Garnier, A. Nikolaus, and P. Sagaut, *Large Eddy Simulation for Compressible Flows*. Springer, 2009 ed., 2009.

[20] A. Montorfano, F. Piscaglia, and A. Onorati, "Wall-adapting subgrid-scale models to apply to large eddy simulation of internal combustion engines," *International Journal of Computer Mathematics*, vol. 0, no. 0, pp. 1–9, 2013.

[21] H. K. Versteeg and W. Malalasekera, *An Introduction to Computational Fluid Dynamics*. Prentice Hall College Div, 2nd edition, 2007.

[22] H. Weller, "Controlling the computational modes of the arbitrarily structured C grid," *Monthly Weather Review*, vol. 140, pp. 3220–3234, 2012.

[23] D. Dietzel, D. Messig, F. Piscaglia, A. Montorfano, G. Olenik, O. Stein, A. Kronenburg, A. Onorati, and C. Hasse, "Evaluation of scale resolving turbulence generation methods for large eddy simulation of turbulent flows," *to appear in Computers & Fluids*, 2014.

[24] L. Sirovich, "Turbulence and the dynamic of coherent structures," *Quarterly of Applied Mathematics*, vol. 45, pp. 561–590, 1987.

[25] G. Berkooz, P. Holmes, and J. L. Lumley, "The proper orthogonal decomposition in the analysis of turbulent flows," *Annual Review of Fluid Mechanics*, vol. 25, no. 16, pp. 539–575, 1993.

[26] A. A. Fogleman, K. Lumley, D. Rempfer, and D. C. Haworth, "Application of the proper orthogonal decomposition to datasets of internal combustion engine flows," *Journal of Turbulence*, vol. 5, no. 23, pp. 1–18, 2004.

[27] K. Liu and D. C. Haworth, "Development and assessment of POD for analysis of turbulent flow in piston engines," *SAE technical paper 2011-01-0830*, 2011.

[28] M. Schmitt, C. E. Frouzakis, A. G. Tomboulides, Y. M. Wright, and K. Boulouchos, "Direct numerical simulation in engine-like geometries." Physics of fluids (submitted), 2014.

[29] F. Brusiani and G. M. Bianchi, "Basic numerical assessments to perform a quasi-complete les toward ic-engine applications," in *Proceedings of the ASME 2010 International Mechanical Engineering Congress & Exposition*, IMECE2010, (Vancouver, British Columbia, Canada), November, 12-18 2010.

[30] F. Brusiani, C. Forte, and G. Bianchi, "Assessment of a numerical methodology for large eddy simulation of ICE wall bounded non-reactive flows," in *SAE Technical Paper 2007-01-4145*, 2007.